Journal of Materials Chemistry C

Defect-induced formation and frustration driven multiple magnetic transitions in $Gd_2Co_{0.90}Si_{2.90}$

Journal:	*Journal of Materials Chemistry C*
Manuscript ID	TC-ART-05-2024-001798.R1
Article Type:	Paper
Date Submitted by the Author:	25-Jun-2024
Complete List of Authors:	Kundu, Mily ; Saha Institute of Nuclear Physics, Condensed Matter Physics Division Pakhira, Santanu; Maulana Azad National Institute of Technology, Physics Gupta, Shuvankar; Saha Institute of Nuclear Physics, Condensed Matter Physics Choudhary, Renu; Ames Laboratory Sarkar, Sourav; S N Bose National Centre for Basic Sciences, Condensed Matter and Materials Physics Laksnarasimhan, N.; CECRI, Functional Materials Ranganathan, R.; Saha Institute of Nuclear Physics, Condensed Matter Physics Division Mandal, Kalyan; S N Bose National Centre for Basic Sciences, Physical Sciences Johnson, Duane; Iowa State University, Materials Science and Engineering; Ames Laboratory, Mazumdar, Chandan; Saha Institute of Nuclear Physics, Condensed Matter Physics Division

Journal Name

ARTICLE TYPE

Cite this: DOI: 00.0000/xxxxxxxxxx

Defect-induced formation and frustration driven multiple magnetic transitions in $Gd_2Co_{0.90}Si_{2.90}$

Mily Kundu[a,b], Santanu Pakhira[c,*], Shuvankar Gupta[b], Renu Choudhary[d], Sourav Sarkar[a], N. Lakshminarasimhan[e,f], R. Ranganathan[b], Kalyan Mandal[a], Duane D. Johnson[d,g], and Chandan Mazumdar[b]

Received Date
Accepted Date

DOI: 00.0000/xxxxxxxxxx

A new ternary compound $Gd_2Co_{0.90}Si_{2.90}$ has been synthesized in chemically single phase by deliberately introducing lattice vacancies in the Co and Si sites. The system is characterized through dc magnetization, heat capacity, resistivity along with density functional theory (DFT) calculations. A detailed experimental study reveals that the system exhibits an antiferromagneic transition below $T_N = 11.3$ K followed by spin freezing behaviour below $T_B \sim 4.8$ K. An additional high-temperature magnetic transition could also be detected at $T_H \sim 150$ K, which is short range in character and is associated with defect-induced polarization of the conduction electrons. The spin-glass-like state formation in the system is additionally bolstered by the observation of magnetic relaxation and associated aging phenomena as well as magnetic memory effect. On the basis of non-equilibrium dynamical behaviour, we argue that the glassy state in this compound favours the hierarchical model over the droplet model. DFT calculations as well as experimental outcomes establish that the ground state is magnetically frustrated due to small energy difference between distinct spin configurations having closely spaced ground-state energies.

1 Introduction

Magnetically frustrated systems with highly degenerate ground states always offer a fertile ground for exploring novel magnetic and electronic states [1–12]. Magnetic frustration occurs when the configuration of magnetic moments (spins) in a crystal lattice is restricted by the crystal structure or competing interactions, hindering it from aligning in a unique direction. Furthermore, the existence of local structural disorder is also conducive to the frustration by weakening the long-range nature of magnetic interaction and triggers the system into a spin-freezing state through finding a local free energy minima [13–15]. In the absence of substantial disorder, novel magnetic states like spin-ice and spin-liquid states can also be facilitated in the concerned system [16–19]. Such spin states are reported to exhibit a range of unusual properties, many are of current interest, such as topological order, fractional excitations [20,21]. Recently, skyrmion-like topological spin-textures are also observed in magnetically frustrated systems, where frustration plays a crucial role for the development of such vortex-like spin texture [22–24]. Such topological spin-textures have potential applications in spintronics and data storage due to their stability and the ease with which they can be manipulated using magnetic fields [25–28]. Thus, besides helping us in resolving the underlying origins of fundamental physics, magnetically frustrated systems can also find numerous technological applications in fields such as data storage, spintronics, and quantum computing. As such, the exploration of magnetic frustration remains a vibrant field of study in condensed matter physics, yielding regular discoveries and insights.

One potential class of magnetically frustrated materials are R_2TX_3 (R = rare-earth, T = transition elements and X = p block elements) type of compounds, which have drawn considerable attention due to its captivating characteristics such as Kondo effects, various magnetic transitions, magnetic frustration, and spin-glass behaviors, as well as mixed-valence state, significant magnetocaloric effects, magnetic memory effects, and dynamical susceptibility with bidirectional frequency dependence, etc [1,4,5,9,29–37]. These compounds form in hexagonal AlB_2-type crystal structure. Gd_2PdSi_3 is one such member that is recently discovered to host

[a] Department of Condensed Matter and Materials Physics, S. N. Bose National Centre for Basic Sciences, Block JD, Sector III, Salt Lake, Kolkata 700106, India
[b] Condensed Matter Physics Division, Saha Institute of Nuclear Physics, 1/AF Bidhannagar, Kolkata 700064, India
[c] Department of Physics, Maulana Azad National Institute of Technology Bhopal 462003, India
[d] Ames National Laboratory, Iowa State University, Ames, Iowa 50011, USA
[e] Electro-organic and Materials Electrochemistry Division, CSIR-Central Electrochemical Research Institute, Karaikudi 630 003, India
[f] Academy of Scientific and Innovative Research (AcSIR), Ghaziabad 201 002, India
[g] Department of Materials Science and Engineering, Iowa State University, Ames, Iowa 50011, USA
* spakhira.phy@gmail.com

skyrmionic spin state having a centrosymmetric crystal structure, where magnetic frustration drives the topological spin texture formation in the absence of Dzyaloshinskii–Moriya interaction[38]. Following the discovery of magnetic skyrmion in Gd_2PdSi_3, flurries of research activities has been directed towards exploring different structurally related compounds and studying their magnetic spin structure and interactions. One prime example is the recent report on R_2RhSi_3 (R = Gd, Tb, and Dy)[39] which shows magnetic and transport anomalies vis-à-vis those observed in Gd_2PdSi_3 and are claimed to be related to the presence of magnetic frustration. Another recent work on $Gd_2Ir_{0.97}Si_{2.97}$[40] suggests that the material possesses a large number of possible magnetic configurations, resulting in a highly degenerate ground state with complex magnetic behavior.

In this study, we detail the synthesis of a novel member $Gd_2Co_{0.90}Si_{2.90}$, having rather close similarities in both crystal structure as well as constituent elements with those of Gd_2PdSi_3, and have studied its structural, magnetic and transport properties. Multiple magnetic transitions are noticed in the crystallographically single phase compound. Our experimental investigations, coupled with theoretical analysis, reveal the competitive dynamics among various spin configurations, giving rise to pronounced spin frustration. This, in conjunction with bond disorder, culminates in a magnetically frustrated glassy behavior at low temperatures.

2 Experimental and Theoretical Details

Polycrystalline samples were synthesized by arc-melting technique using appropriate amounts of high-purity (purity $\geq$ 99.9 %) constituent elements. The ingots were melted several times to ensure a homogeneous formation of the samples. The powder x-ray diffraction (XRD) measurements of the synthesized samples were performed in a TTRAX-III diffractometer (M/s. Rigaku Corp., Japan). The diffraction pattern was analyzed using FullProf software package[41] for structural characterization. The instrument EVO 18 (M/s. Carl Zeiss, AG, Germany) was utilized for conducting scanning electron microscopy (SEM) measurements, to ensure the homogeneity of the prepared sample, whereas elemental compositions were estimated through energy-dispersive x-ray spectroscopy measurements in a commercial element EDS system (M/s. EDAX, USA). A SQUID VSM (M/s. Quantum Design Inc., USA) was employed to measure the magnetization as a function of temperature and applied magnetic field. Measurements of zero-field heat capacity and resistivity have been conducted through a commercial Physical Property Measurement System (PPMS) (M/s. Quantum Design Inc., USA).

The electronic and magnetic properties of Gd_2CoSi_3 are studied using density-functional theory (DFT). The DFT calculations employ pseudo potential within a projector-augmented wave (PAW) method[60,61], as implemented in the Vienna Ab-initio Simulation Package (VASP)[62]. The Perdew-Burke-Ernzerhof-based generalized gradient approximation (PBE-GGA)[63] is used as exchange-correlational functions. We have applied an onsite electron-correlation (effective Hubbard) parameter $|U-J|$ of 6 eV and spin-orbit coupling (SOC) for strongly correlated Gd-4f states. The low-temperature experimental lattice parameters are used for our DFT calculations. The total-energy convergence criterion for the self-consistent calculations was fixed to 10^{-7} eV per cell, using an energy cutoff of 520 eV for the wave functions. The Brillouin zone integration was performed using a k-point mesh based on the tetrahedron method with Bloch corrections. A Γ-centered grid of 9$\times$ 9$\times$ 6 k-point meshes was used for Brillouin-zone integration.

3 Results and discussions

3.1 Structural details and phase analysis

The XRD pattern of stoichiometric material Gd_2CoSi_3 at room temperature is shown in Fig. 1(a). Full-Rietveld analysis of the diffraction pattern indicates the presence of $\sim$ 10% secondary phase having composition $GdCoSi_2$ in addition to the target phase Gd_2CoSi_3 that can not be removed by thermal annealing. The secondary phase could be removed with the introduction of vacancies in the Co and Si sites, as earlier demonstrated for different other R_2TSi_3 (T = Ni, Co) compounds[34,35,42,43]. The amount of Gd, Co, and Si responsible for forming the secondary phase was calculated and subtracted from the initial amount of Gd, Co, and Si used for the initial stoichiometric synthesis. This results in a non-stoichiometric starting composition $Gd_2Co_{0.90}Si_{2.90}$ (Occupancies in the Co and Si sites were scaled considering full occupancy on the Gd site) and it is found that the compound forms in a single phase without any traceable amount of secondary phase. The structural analysis confirms that the single-phase compound crystallizes in the U_2RuSi_3-type structure with space group *P6/mmm* (Fig. 1(c). In this crystal structure, Gd atoms occupy two independent Wyckoff sites having non-identical atomic environments. Such type of inequivalent Wyckoff symmetries along with the presence of vacancies introduced in the Co and Si sites randomized the effective exchange interaction length among the Gd ions creating a strong bond disorder in the system. The refined composition obtained from the Rietveld analysis is $Gd_2Co_{0.96(1)}Si_{2.96(2)}$ which is in close proximity to the starting composition. The single phase nature as well as the homogeneous character of the material is further confirmed through SEM image captured using back-scattered electron (BSE) (Fig. 2). The elemental composition determined through EDX spectrum analysis for the prepared material is $Gd_2Co_{0.97(2)}Si_{2.90(3)}$, closely resembling both the initial composition and the composition obtained from the Rietveld refinement process. The low-temperature XRD measurements in the temperature range 15 K $\leq T \leq$ 300 K (Fig. 3(a)) rule out the possibility of any structural transition for the compound down to 15 K. The temperature dependence of lattice unit cell volume follows the standard thermal contraction behaviour.

$$V(T) = \frac{\gamma U(T)}{K_0} + V_0 \quad (1)$$

where, V_0 is the zero-temperature unit cell volume, K_0 is bulk modulus, γ is the Grüneisen parameter and internal energy is de-

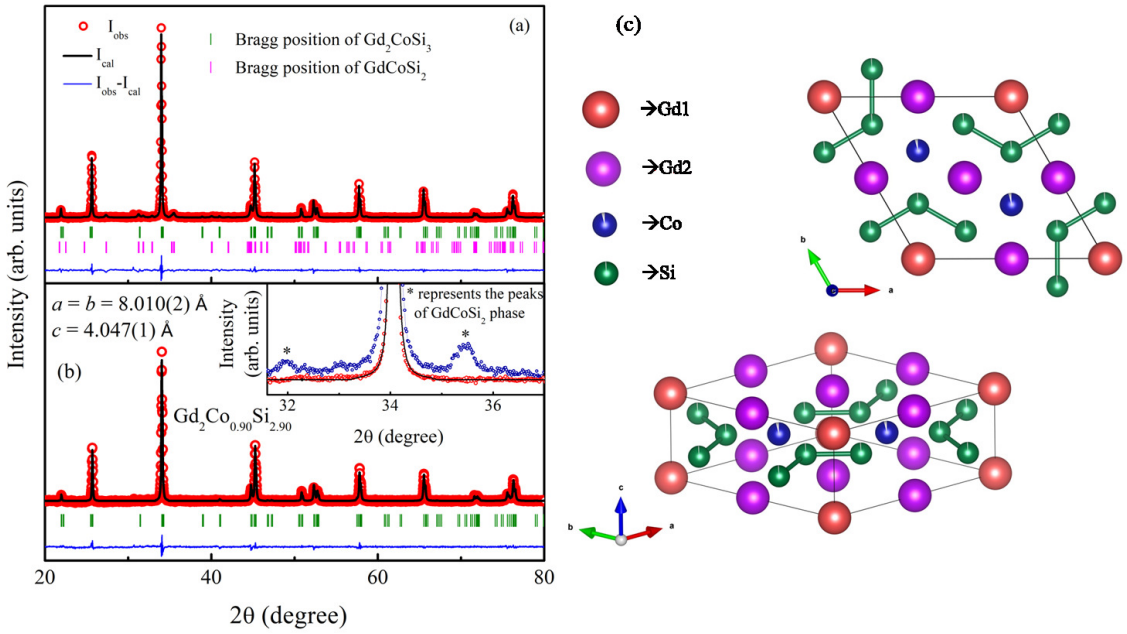

Fig. 1 XRD pattern of the powder samples (a) Gd_2CoSi_3 and (b) $Gd_2Co_{0.90}Si_{2.90}$ along with full-Rietveld refinement at room temperature. Inset present the presence of secondary phase of $GdCoSi_2$ type in Gd_2CoSi_3 (upper), while $Gd_2Co_{0.90}Si_{2.90}$ (lower) form in single phase, devoid of any detectable secondary phase. (c) Crystal structure of $Gd_2Co_{0.90}Si_{2.90}$ belonging to U_2RuSi_3-type structure with space group *P6/mmm*

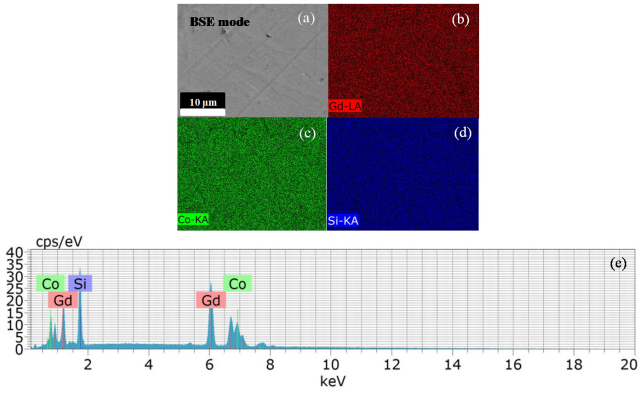

Fig. 2 (a) Backscattered electron (BSE) image and elemental mapping [(b)–(d)] via SEM equipped with EDX on the polished surface of $Gd_2Co_{0.90}Si_{2.90}$ from the depicted region in (a). (e) EDX results of $Gd_2Co_{0.90}Si_{2.90}$.

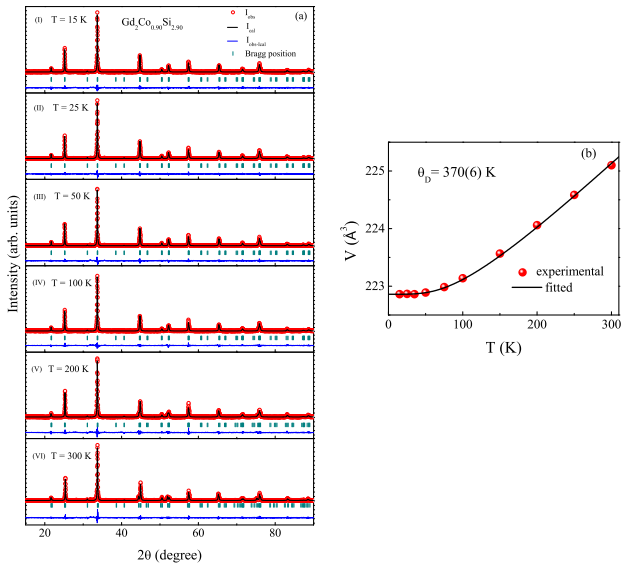

Fig. 3 (a)XRD patterns of $Gd_2Co_{0.90}Si_{2.90}$ at different temperatures with corresponding full-Rietveld refinements. (b) Unit-cell volume as a function of temperature, fitted using Eq. 1.

noted by $U(T)$ which could be expressed by Debye model as

$$U(T) = 9nRT\left(\frac{T}{\theta_D}\right)^3 \int_0^{\theta_D/T} \frac{x^3}{e^x - 1} dx. \quad (2)$$

Here, θ_D represents the Debye temperature and n stands for the number of atoms per formula unit (f.u.). As shown in Fig. 3(b), a good fitting of the temperature-dependent lattice unit-cell volume using eq. 1 yields the Debye temperature to be θ_D= 370(6) K, which is very close to that obtained from the Debye model of heat capacity (section 3.3). This value is quite close to that obtained for different other isostructural compounds[5,34,42].

3.2 DC Magnetization

The variation in dc magnetic susceptibility with temperature ($\chi \equiv M/H$) for $Gd_2Co_{0.90}Si_{2.90}$ measured at $H = 1$ kOe, under both zero-field-cooled (ZFC) and field-cooled (FC) protocols are shown in Fig. 4(a) (left panel). The compound exhibits two separate magnetic transitions at lower temperatures. The magnetic ordering appears to be antiferromagnetic (AFM)-type at $T_N = 11.3$ K, while the low-temperature transition around T_B =

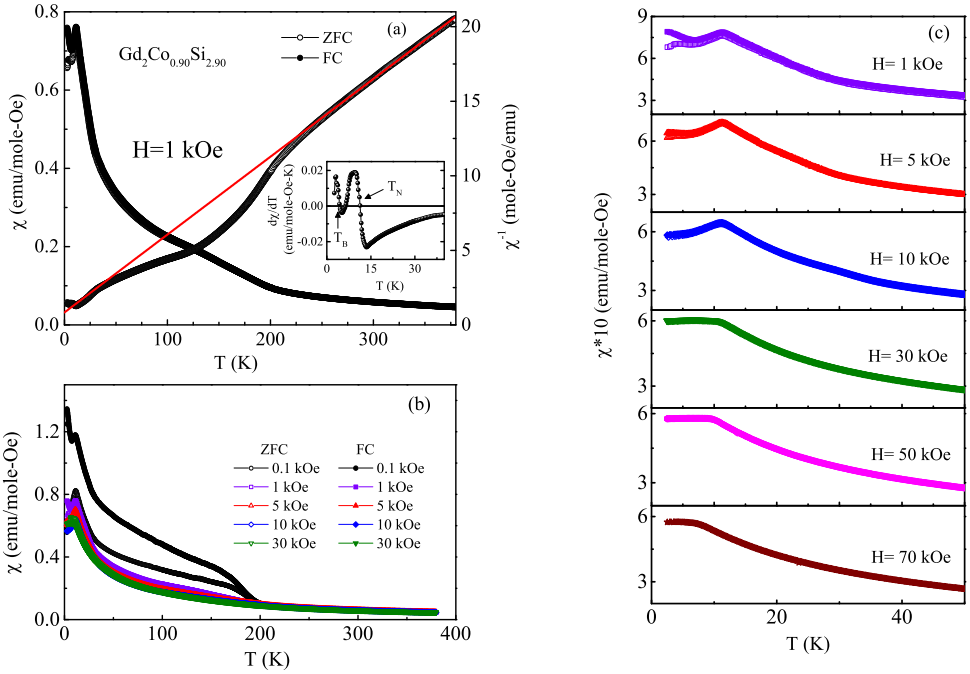

Fig. 4 (a) Dc magnetic susceptibility as a function of system temperature for magnetic field $H = 1$ kOe. The red line corresponds to Curie-Weiss fitting in the high temperature region and it is extrapolated down to 0 K. (b) Temperature dependent dc magnetic susceptibility (χ) for different magnetic fields. Inset presents first order time derivative of magnetic susceptibility. (c) Variation of magnetic susceptibility in the low-temperature region for different magnetic fields

4.8 K is manifested as a relatively broader peak in the $\chi(T)$ data. Magnetic susceptibility recorded under various applied magnetic fields is plotted in Fig. 4(b). Similar multiple transitions are also observed for many other structurally related compounds, where a spin-glass state emerges beneath an antiferromagnetic (AFM) ordered state due to the elevated degeneracy of magnetically frustrated ground states[42–44]. Similar to those isostructural compounds, here too a persistent bifurcation is observed between the ZFC and FC magnetic susceptibility up to higher fields around T_B (Fig. 4(a-c)), signifying the metastable short-range nature of the magnetic transition.

In these materials exchange interaction between the localized rare-earth (R) ions is Ruderman–Kittel–Kasuya–Yosida (RKKY) type, which is mediated through conduction electrons and oscillatory in nature depending upon the interatomic distances. In the case of $Gd_2Co_{0.90}Si_{2.90}$, the non-identical atomic environments create bond-disorder in the system along the R-R exchange path. The presence of such types of bond-disorder along with the presence of atomic vacancies in the Ni/Si sites are responsible for the variation of local electronic environments in the system between the R ions and results in competing exchange interactions in the system between nearest-neighbor and next-nearest-neighbor localized spins. Additionally, the presence of defects on the Co and Si sites is also responsible for the conduction carrier blocking by creating voids in the R-R exchange interaction path. As a combined contribution of these, the system is magnetically frustrated with different possible competing ground state spin configurations having equivalent energies. As a result, although the system exhibits an AFM transition below T_N, competing interactions (that may come from higher-order neighbours) also develop gradually with lowering the temperature, and as a consequence, the system undergoes a glassy state formation below T_B.

In addition to these transitions at low temperatures, one may find a signature of another weak magnetic transition at a high temperature $T_H \sim 150$ K, which gets suppressed with an increase in H. No secondary phases, capable of causing the observed high-temperature anomaly in magnetic susceptibility, were identified through XRD and EDAX data analyses. On the other hand, a similar feature had also been detected earlier in some other isostructural as well as structurally related compounds, where it was shown that such high-temperature transition is not associated with any additional phase in the system and rather intrinsic to it, which may originate due to the defect-induced polarization of the conduction electrons[34,35,40]. This anomaly, however, could be suppressed rather easily by applying a moderately high externally applied magnetic field. Such high-temperature short-range magnetic correlation above the long-range magnetic ordering in this system with site defects could manifest a Griffith-like phase[11,45], which is not addressed in this work.

To estimate the effective paramagnetic moment (μ_{eff}) of the system of interest, the inverse magnetic susceptibility data for $H = 1$ kOe in the temperature range 240-380 K, is fitted with the help of Curie-Weiss (CW) law $\chi = C/T - \theta_p$, as shown in Fig. 4(a)(right panel). The fitting yields the paramagnetic Curie temperature $\theta_p = -16.7$ K and $\mu_{eff} = 12.40$ μ_B/f.u. If the magnetic interaction is primarily due to the localized Gd-4f electrons, the effective moment anticipated to closely match the theoretical value of 11.23 μ_B/f.u., considering the presence of 2 Gd atoms

in the formula unit. The slightly elevated estimated value of μ_{eff} suggests an additional contribution coming from the d electrons as well, akin to that found out in many members of R_2TX_3 series[34,35].

Enhancement of the applied magnetic field strongly suppresses the low-temperature transition at T_B. However, the peak in the magnetic susceptibility at T_N is still observable even at $H = 70$ kOe, although the peak position moves to a lower temperature as the field strength increases (Fig. 4(c)). This is consistent with the field-dependent isothermal magnetization measurements performed below T_N (Fig. 5), where almost linear $M(H)$ behavior is observed up to $H = 70$ kOe without a saturation tendency. This suggests the presence of dominant long-range AFM ordering in the system at T_N. The combined results of magnetic susceptibility and field-dependence of isothermal magnetic measurements indicate that multiple magnetic phases coexist in the system, two short-range in nature around T_H and T_B, along with one long-range ordered phase at T_N. Similar magnetic phase inhomogeneity are also reported for isostructural compounds $Sm_2Ni_{0.87}Si_{2.87}$, Er_2NiSi_3, $Tb_2Ni_{0.90}Si_{2.94}$, $Nd_2Co_{0.85}Si_{2.88}$[35,43,44,46]. The short-range ordered states are metastable in nature and easily get spin-polarized in the field direction with increasing H. Moreover, the long-range AFM-ordered state is quite dominant restricting the overall ferromagnetic polarization within the system until $H = 70$ kOe.

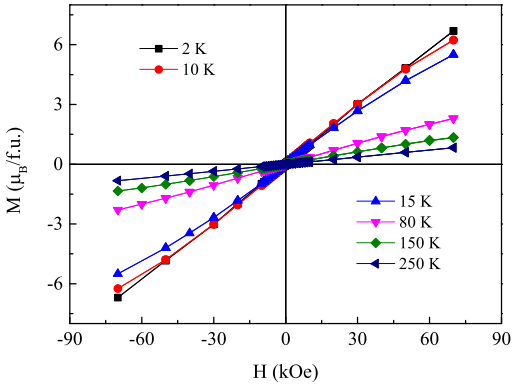

Fig. 5 Variations in magnetization with respect to magnetic field observed at different temperatures.

3.3 Heat capacity

To comprehend the magnetic transitions observed at different temperatures, zero-field heat capacity (C_p) measurements have been carried out for $Gd_2Co_{0.90}Si_{2.90}$. A lambda (λ)-like peak around $T_N = 11.3$ K is observed in the $C_p(T)$ behavior along with an additional hump around $T_B \sim 4.8$ K, as shown in Fig. 6. This also indicates the formation of long-range ordering within the system below T_N, whereas the magnetic transition below T_B is short-range in nature. The magnetic contribution (C_{mag}(T)) correlated with the localized 4-f electrons of Gd ions can be determined by subtracting the heat capacity of the isostructural analogue $La_2Co_{0.99}Si_{2.99}$ with suitable adjustment for lattice volume[47]. As can be seen from Fig. 6, a clear sharp peak is observed in the C_{mag}(T) data associated with the long-range AFM ordering of Gd^{3+} spins with $S = 7/2$, while the weak hump around T_B is due to the short-range ordering associated with lower magnetic entropy. The magnetic entropy has been calculated using the relation $S_{mag} = \int_0^T \frac{C_{mag}}{T} dT$. The estimated value of S_{mag} at T_B and T_N are about 28% and 81%, respectively, of expected theoretical value $Rln(2J+1) = 17.289$ J/mole-Gd-K. The notably low value in the vicinity of T_B is quite consistent with the system's glassy characteristics as identified in the non-equilibrium investigation (section 3.5). The reduced value of magnetic entropy at T_N suggests that it is plausible that a majority of the magnetic ions contribute to the ordering process, while the remaining ones exhibit frustrated characteristics, playing a role in the emergence of the glassy phase at lower temperatures. The full entropy is released at temperatures significantly greater than T_N, signifying the existence of short-range magnetic interactions above long-range magnetic ordering.

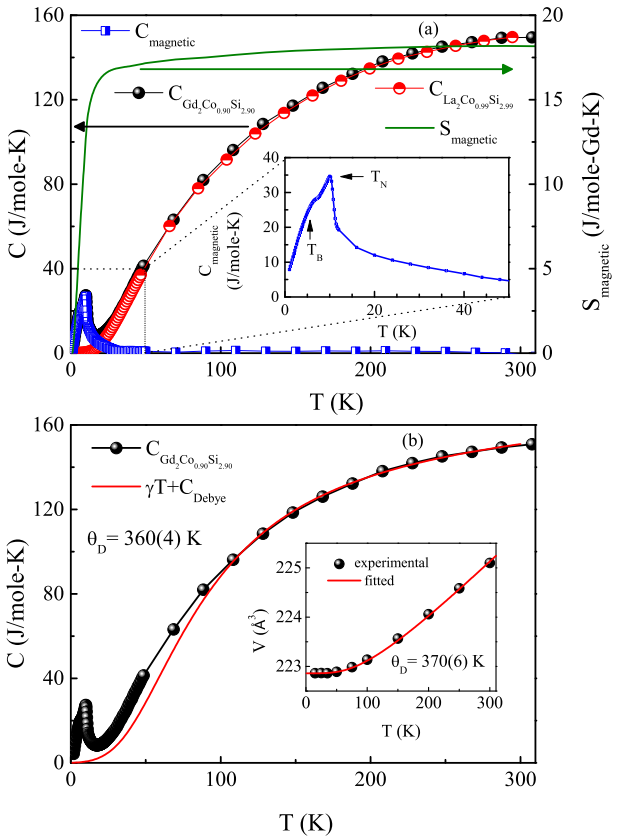

Fig. 6 (a) (Left panel) Zero-field heat capacity (C(T))of $Gd_2Co_{0.90}Si_{2.90}$ and its non-magnetic analogue $La_2Co_{0.99}Si_{2.99}$ in the temperature range 2-300 K, along with estimated magnetic contribution of heat capacity ($C_{magnetic}$). (Right panel) Calculated magnetic entropy ($S_{magnetic}$) as a function of temperature. Inset presents the magnetic contribution in an expanded view. (b) Heat capacity of $Gd_2Co_{0.90}Si_{2.90}$ fitted using Debye model. Inset presents temperature dependence of lattice unit cell volume fitted through corresponding Debye model.

The heat-capacity data of $Gd_2Co_{0.90}Si_{2.90}$ can be fitted using the Debye model in which the lattice contribution (phonon) to heat

capacity could be expressed as[48]

$$C_{\rm D}(T) = 9nR\left(\frac{T}{\theta_{\rm D}}\right)^3 \int_0^{\theta_{\rm D}/T} \frac{x^4 e^x}{(e^x-1)^2} dx. \quad (3)$$

Here n denotes the atom count per formula unit and $x = \theta_{\rm D}/T$, where $\theta_{\rm D}$ is the Debye temperature. The best fit is obtained with $\theta_{\rm D} = 360(4)$ K. A large number of intermetallic[34,46,49,50], as well as oxide[51] compounds are reported earlier to have $\theta_{\rm D}$ in the similar temperature range in the absence of any magnon contribution.

3.4 Resistivity

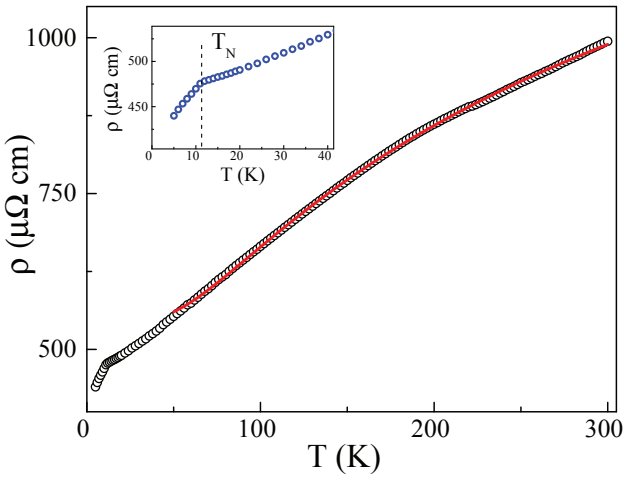

Fig. 7 Variation in resistivity (ρ) with temperature for $Gd_2Co_{0.90}Si_{2.90}$. Inset presents the enlarged view of low temperature region. Black open circles represent experimental data and the red line is the fitted data using equation 4.

To further investigate different magnetic transitions observed in the system, the temperature dependence of electrical resistivity ρ(T) of $Gd_2Co_{0.90}Si_{2.90}$ is measured in the temperature regime 5-300 K in absence of magnetic field taken in both cooling and heating cycle (for clarity of the images only heating cycle data presented here in Fig. 7). No irreversibility between the heating and cooling cycle in the ρ(T) behaviour is observed around the observed transitions in the system, which is consistent with the absence of structural transition at T_N in the studied compound. The resistivity rises as the temperature increases and shows a typical metallic behaviour throughout the measurement regime. A sharp variation in the gradient of ρ(T) is seen at 11 K while a weak but discernible slope change is also observed near 200 K. Both of these anomalies are consistent with the observed magnetic transition. The rapid decrease in the resistivity below T_N is due to the reduction in spin disorder scattering, resembling what was noted in the case of isostructural compound $Gd_2Ir_{0.97}Si_{2.97}$[40]. In addition to the manifestation of various transitions in the same line, as that observed in the magnetic and heat capacity behavior, it is important to note that the resistivity value of the studied compound is relatively high compared to that for the majority of other R_2TX_3 systems. The estimated residual resistivity ratio (RRR) is also low 2.26. Thus, it is conceivable that the metallic nature of the material is far from ideal. The resistivity data in the temperature region 50–300 K can be described using the parallel resistor model[52]

$$\frac{1}{\rho(T)} = \frac{1}{\rho_1(T)} + \frac{1}{\rho_{max}(T)} \quad (4)$$

where ρ_{max} is the saturation resistivity that is independent of temperature and $\rho_1(T)$ is the ideal temperature-dependent resistivity. The ideal resistivity is given by the following expression:

$$\rho_1(T) = A\left(\frac{T}{\Theta_D}\right)^5 \int_0^{\frac{\Theta_D}{T}} \frac{x^5}{(e^x-1)(1-e^{-x})} dx \quad (5)$$

where A is the phonon scattering constant and Θ_D is the Debye temperature. The fit yielded Θ_D = 355 K, approximating the value obtained through heat capacity fitting.

3.5 Non equilibrium dynamics

3.5.1 Magnetic relaxation and ageing effect

The development of a spin-glass state below T_B is confirmed through the non equilibrium behaviour of the system below the temperature T_B. There are a huge number of frozen configurations present in a glassy state and the system undergoes gradual evolution from one such state to the energetically adjacent state with time. The time required to attain thermal equilibrium when subjected to an external magnetic field is too high and the time required for the relaxation process is referred to as the relaxation time. In order to verify the existence of such frozen magnetic states in our system, the sample was initially cooled from a paramagnetic state to a specific temperature below T_B, without any magnetic field. Subsequently, a rather small magnetic field (100 Oe) was applied following the stabilization of temperature (over a waiting time t_w) and the ZFC magnetization ($M(t)$) was recorded for $\sim$ 7200 sec. We have plotted all the $M(t)$ data after normalization relative to the initial magnetization ($M(0)$) at $t = 0$ i.e. in the form of $M(t)/M(0)$. The time-dependent magnetization data ($M(t)/M(0)$) as shown in Fig. 8(a), has been fitted using the stretched exponential function

$$M(t) = M_0 \pm M_g \exp\left[-\left(\frac{\rm t}{\tau}\right)^{\beta}\right] \quad (6)$$

where M_0 is the intrinsic FM component, M_g is the glassy component of magnetization, τ is the characteristic relaxation time and β is the stretching parameter. It is observed that the magnitude of $\beta = 0.31$ lies in a comparable range of other glassy materials belonging to R_2TSi_3 series[35,42,43]. The estimated value of τ increases with a rise in t_w indicating that the spins are becoming more stiffened, exhibiting ageing phenomenon. The phenomenon of aging can be depicted in a more convenient manner by finding the relaxation rate

$$S(t) = \frac{1}{H}\frac{dM(t)}{d(\log t)} \quad (7)$$

which shows that the apex in the $S(t)$ curve moves towards an extended observation time. as t_w increases(Fig. 8(b)) that indicates the nonequilibrium dynamics of domain growth in the system.

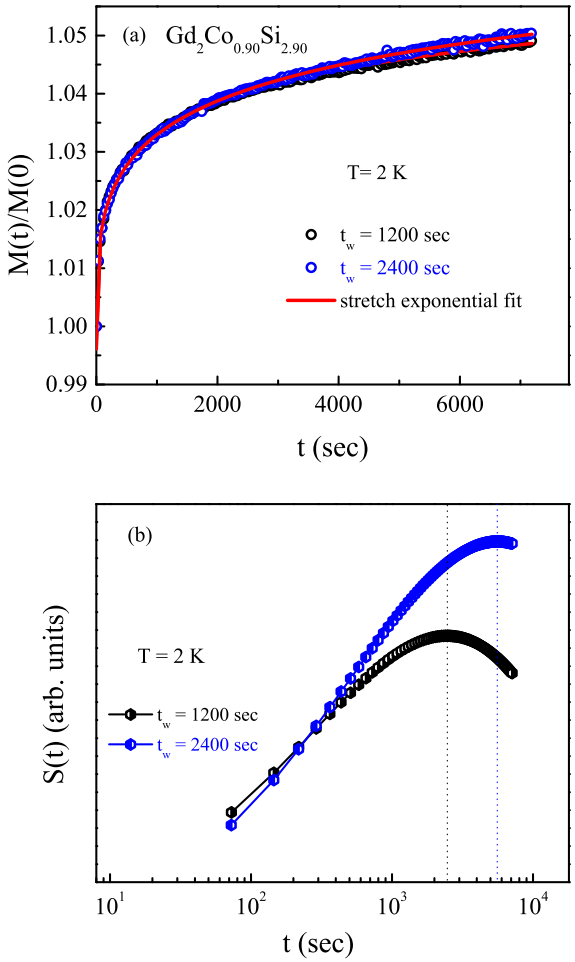

Fig. 8 (a) Temporal variation in the normalized magnetization of $Gd_2Co_{0.90}Si_{2.90}$ at T = 2 K under the ZFC protocol for varying wait durations, accompanied by a fit using a stretched exponential model (Eq. 6). (b) The relaxation rate $S(t)$ at T = 2 K for two different wait times in ZFC protocol for $Gd_2Co_{0.90}Si_{2.90}$, exhibiting aging phenomenon.

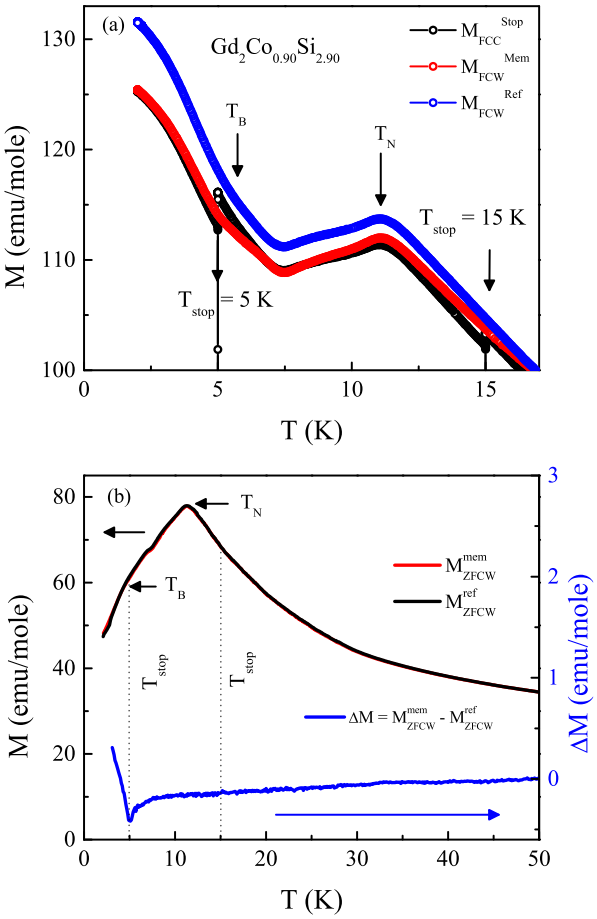

Fig. 9 Magnetic memory effect of $Gd_2Co_{0.90}Si_{2.90}$ in (a) field-cooled (FC) condition and (b) zero-field-cooled (ZFC) condition for 100 Oe applied field.

3.5.2 Magnetic memory effect

The investigation of memory effect has been conducted in both field-cooled (FC) and zero-field-cooled (ZFC) modes, adhering to the protocol established by Sun *et. al*[53]. In FC protocol, the sample was initially cooled down from the paramagnetic region (300 K) to the lowest temperature (2 K) under the application of 100 Oe magnetic field with intermittent stops at T_{stop} = 15 K and 5 K for t_w = 1 hr, during which the magnetic field was switched off. After the lapse of wait-time t_w, the same field was reapplied to the sample at each stop-temperatures and cooling was resumed. Magnetization measured in this process is presented as M_{FCC}^{stop} in Fig. 9(a). After attaining 2 K, the sample was warmed up continuously up to 300 K with the same applied field and the corresponding magnetization data is depicted as M_{FCW}^{mem}. There is a tendency of the memory curve (M_{FCW}^{mem}) to follow the M_{FCC}^{stop} curve at 5 K but it is not emphasized at 15 K, which implies that the system has memory effect at 5 K but the effect disappeared at 15 K. It is worth noting that the memory effect in FC protocol can also result for a phase-separated or superparamagnetic system[54], whereas the memory effect is observed exclusively in authentic spin-glass systems during both the FC and ZFC processes. To identify the actual origin of the memory effect, the measurement has also been conducted in the ZFC protocol, where the sample was first continuously zero-field cooled without an external magnetic field, from the paramagnetic region to specific selected stopping temperatures (T_{stop} = 15 K and 5 K) applying a stopping time of 1.5 hr at each of the T_{stop}s. Subsequently, the cooling process was continued until reaching 2 K, followed by reheating the sample and recording the magnetization under a 100 Oe magnetic field. This $M(t)$ curve is designated as M_{ZFCW}^{mem} (Fig. 9(b)). The typical ZFC magnetization at 100 Oe was also documented and presented as M_{ZFCW}^{ref} in Fig. 9(b). The difference curve, $\Delta M = M_{ZFCW}^{mem} - M_{ZFCW}^{mem}$ exhibits memory dip at 5 K which is in close proximity to T_B, but no such dip was found at 15 K (above T_B). Such a characteristic feature is quite consistent with the FC memory data and confirms the glassy-state formation. The basic ingredients for a spin glass state formation are disorder or randomness, competing interactions, and associated frustration, which are all present in $Gd_2Co_{0.90}Si_{2.90}$ that cause multiple numbers of possible ground state spin configurations having

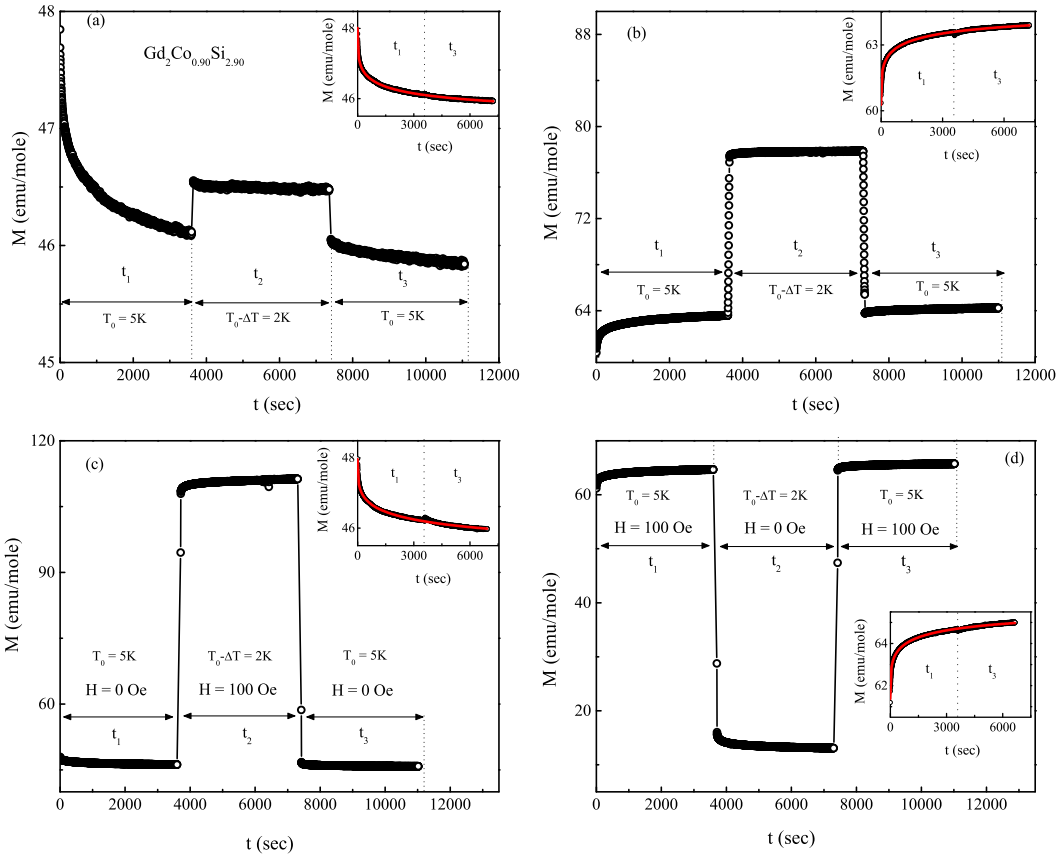

Fig. 10 Magnetic relaxation characteristics of $Gd_2Co_{0.90}Si_{2.90}$ at 5 K under H = 100 Oe with temporary cooling at 2 K, demonstrated through (a) FC method and (b) ZFC method. Magnetic relaxation behaviour at 5 K, featuring a reverse relaxation during temporary cooling at 2 K employing (c) the FC and (d) ZFC protocol. The insets display the relaxation data correlated with the total time elapsed at 5 K, accompanied by the fit (solid red line) employing a stretched exponential function [Eq. 6].

equivalent energies. The presence of local disorder helps the system to freeze in a short-range ordered state with a local minimum in the free energy landscape. Randomness/disorder which is essential to have a glassy system, can be introduced either as site-randomness or as bond-randomness. The crystal structure of $Gd_2Co_{0.90}Si_{2.90}$ is conducive of bond-disorder, as discussed earlier. Additionally, atomic vacancies also contribute to breaking the magnetic periodicity creating additional local disorder in the system, causing the system to freeze in a short-range ordered glassy state.

In general, two models can be employed to explain the memory effect observed in a glassy system, namely, the droplet model[55–57] and the hierarchical model[58,59]. According to the droplet model, the system favors only a single equilibrium spin configuration at a particular temperature, leading to the restoration of the original spin configuration during both temporary heating and cooling. However, the hierarchical model supports an infinite number of metastable states in the free-energy landscape and as a result, the original spin configuration cannot be restored in temporary heating. In order to understand the mechanism demonstrated by our system, we examined the impact of temperature cycling on magnetic relaxation behavior following the protocol proposed by Sun *et. al.*[53]. The relaxation response during temporary cooling under ZFC and FC conditions is illustrated in Figs. 10(a) and 10(b), respectively. In the ZFC technique, the sample was brought to a lower temperature of $T_0 = 5$ K from paramagnetic region in the absence of external magnetic field. Then a small field 100 Oe was applied and magnetization ($M(t)$) was recorded for $t_1 = 1$ hr. After the lapse of t_1, the sample was cooled to a much lower temperature $T_0 - \Delta T = 2$ K in the similar field strength and $M(t)$ was documented for another $t_2 = 1$ hr time. Ultimately, the sample temperature was elevated to T_0, and the measurement of $M(t)$ was conducted for an additional time $t_3 = 1$ hour. In the FC method, the sample was initially cooled from the paramagnetic region to T_0 under the influence of a 100 Oe magnetic field. After reaching T_0, the field was switched off and $M(t)$ was measured following a similar process as of ZFC. It can be observed from Fig. 10 that when the system temperature is restored to T_0, the magnetization returns to the level it attained before temporary cooling in both ZFC and FC processes. One may easily notice that the relaxation curve during t_3 is an extension of that observed during t_1 (insets of Fig. 10(a) and 10(b)) and the combined curve can be fitted well with Eq. 6. The strength of the memory phenomenon has been examined through the investigation of oppo-

site relaxation behaviour by toggling the applied field on and off alternatively in both FC and ZFC methods. Magnetization was measured by keeping the magnetic field switched off during t_1 and t_3 while a 100 Oe field was applied to the system during t_2 in FC process (Fig. 10(c)). In ZFC process, $M(t)$ was measured in the presence of a magnetic field during t_1 and t_3, while the field remained deactivated throughout t_2 and the data has been shown in Fig. 10(d). It is indeed interesting to figure out that instead of reverse relaxation during t_2, the magnetic relaxation behaviour during t_3 almost preserves a sense of continuity, as shown in the insets of Fig. 10(c) and 10(d), and can be well described through the stretched exponential relation (Eq. 6). This kind of behaviour implies a strong memory of the studied system below T_B [35,43].

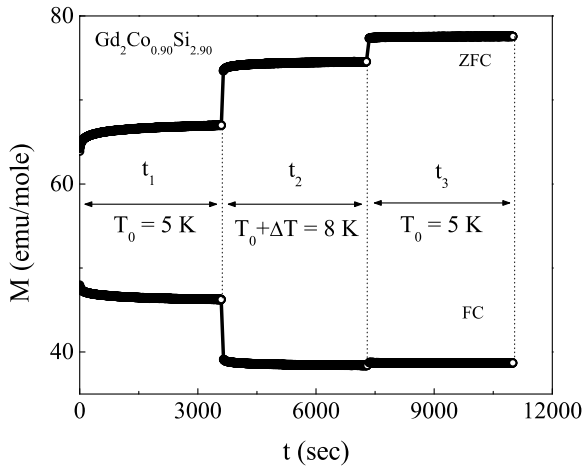

Fig. 11 Magnetic relaxation behaviour of $Gd_2Co_{0.90}Si_{2.90}$ at 5 K with temporary heating at 8 K measured using ZFC and FC protocol for H = 100 Oe.

We have additionally examined the magnetic relaxation behavior during temporary heating to find out whether the original spin configuration is restored akin to temporary cooling or not, while restoring the system temperature. The impact of positive temperature cycling on the magnetic relaxation behavior is depicted in Fig. 11. In the ZFC method, the sample was zero-field-cooled from the paramagnetic region down to $T_0 = 5$ K which is close to T_B. Then a small magnetic field of 100 Oe was applied to the sample and magnetization ($M(t)$) was recorded for $t_1 = 1$ hr. Following this, the sample was momentarily heated to $T_0 + \Delta T = 8$ K under the same field strength, and $M(t)$ was documented for an additional time period, $t_2 = 1$ hour. Finally, the system temperature was again brought down to T_0 and magnetization was measured for time period $t_3 = 1$ hr. It is clearly observed from the figure that the value of magnetization at the beginning of t_3 is quite different from the value it had reached just before temporary heating i.e. during t_1. Equivalent magnetic relaxation behavior was noted in the FC method as well (Fig. 11). Thus the system cannot restore its previous spin-configuration during temporary heating, either in ZFC or FC protocol, which implies the absence of memory in the positive temperature cycling. The asymmetrical nature of magnetic relaxation upon heating and cooling suggests that our system $Gd_2Co_{0.90}Si_{2.90}$ favours the hierarchical model of magnetic relaxation.

3.6 Computational Results

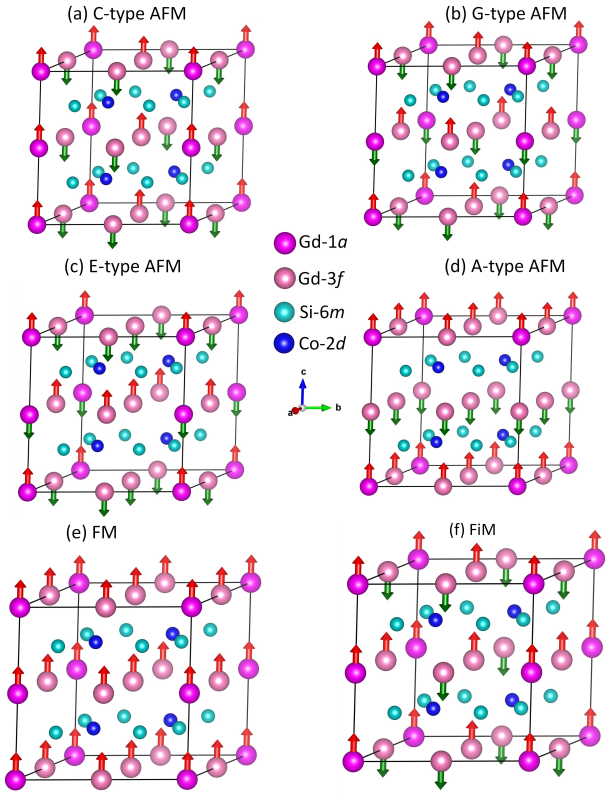

Fig. 12 The studied magnetic configurations in Gd_2CoSi_3 system (a) C-type AFM, (b) G-type AFM, (c) E-type AFM, A-type AFM, (e) Ferromagnetic (FM) and (f) Ferrimagnetic (FiM).

To determine the magnetic properties of the Gd_2CoSi_3 system, we used a $1\times$ $1\times$ 2 supercell. As experimentally observed, the system has zero saturated magnetic moments per cell at low temperatures, meaning that the system is antiferromagnetic (AFM). The spin frustration is a key point of a spin glass [13]. Therefore, to have an insight into spin frustration, different types of AFM configurations, i.e., C-, G-, E-, and A-type AFM are considered, along with the ferromagnetic (FM) and ferrimagnetic (FiM) configurations (Fig. 12(a-f)).

Among the different AFM configurations, the C-type spin configuration is known to has the lowest ground-state energy. However, we found that although the C-type AFM configuration is energetically the most stable, all the other AFM configurations have competing energies. The energy difference ($\Delta E_{\text{conf.}} = E_{\text{conf.}} - E_{\text{C}}$) between the C-type AFM and G-, E-, A-AFM configurations is 0.3 meV/atom ($\sim$ 3.5 K), 0.44 meV/atom ($\sim$ 5.1 K) and 0.5 meV/atom ($\sim$ 5.8 K), respectively. The difference between the C-type and FM configuration (ΔE_{FM}) is 0.63 meV/atom ($\sim$ 7.3 K). The energy difference between AFM and FM configurations is the largest among all considered configurations but still, the number is very small, indicating the competing nature of AFM and FM magnetism in the system. The energy difference between C-type AFM and FiM

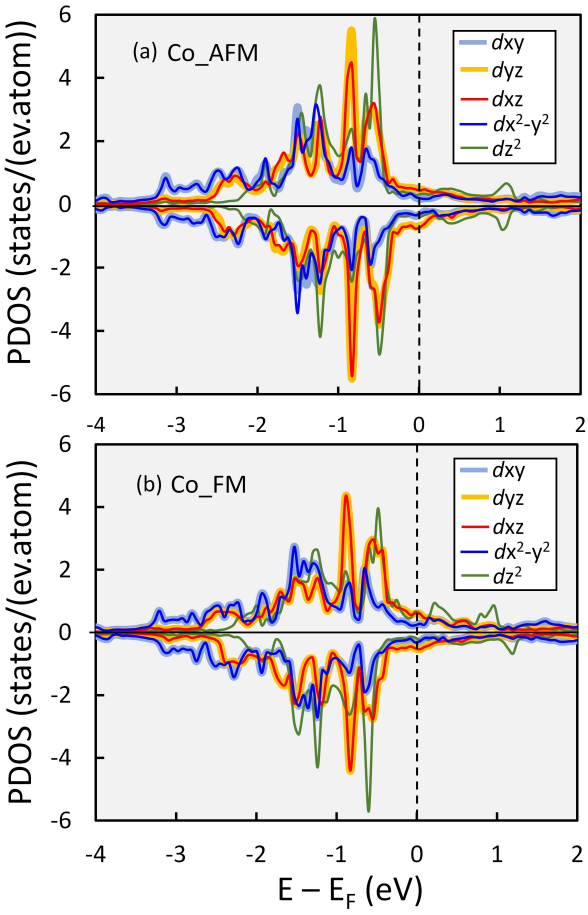

Fig. 13 Partial density of states (PDOS) of Co-atoms in Gd_2CoSi_3 system for (a) antiferromagnetic (AFM) and (b) ferromagnetic (FM) configurations.

configurations (ΔE_{FiM}) is 0.33 meV/atom (~ 3.8 K) which is comparable to ΔE_{G}. This indicates the competing nature of AFM and FiM configurations as well. The small energy difference between all these different spin configurations causes strong spin frustrations. This makes the system very complex where AFM, FM, and FiM configurations compete with each other. The origin of strong spin frustration in $Gd_2Co_{0.90}Si_{2.90}$ lies in its crystal structure that has a planar triangular geometry made of in-plane Gd-Gd ($1a$-$3f$ sites and $3f$-$3f$ sites) equal distances, similar to that reported earlier in structurally related compound $Gd_2Ir_{0.97}Si_{2.97}$ [40]. In $Gd_2Co_{0.90}Si_{2.90}$, Gd-moment per atom is theoretically estimated to be 7.1 μ_{B} per atom in all configurations. The Co-moment is negligible (0.041 μ_{B}) in C-type AFM, and zero in other AFM configurations whereas it has a small value of 0.2 μ_{B} in FM configuration, aligned antiparallel to Gd-moment.

To understand the electronic behavior of cobalt atom, the electronic properties of the system have been explored. Partial density of states (PDOS) i.e. d_{xz}, d_{xy}, d_{yz}, $d_{x^2-y^2}$, and d_{z^2} orbital states, of Co-atom in the C-type AFM and FM configurations are compared in Fig. 13. The orbital states d_{xy} overlap with the $d_{x^2-y^2}$ and d_{yz} states overlap with d_{xz} states in both AFM (Fig. 13(a)) and FM (Fig. 13(b)) configurations. In both configurations, the exchange splitting of Co-states is collapsed at the Fermi level which causes the quenching of the Co-moment [64]. The Co-states show same behavior in FiM configuration, not shown here. The electronic structure of Co-atom in all configurations is almost the same i.e., collapsing of exchange splitting. This corroborates the intricate nature of the magnetization within the system.

4 Concluding Remarks

In this study, we present the successful synthesis and physical characteristics of an new hexagonal intermetallic compound $Gd_2Co_{0.90}Si_{2.90}$ exhibiting multiple magnetic transitions. The compound exhibits an antiferromagnetic transition below $T_{\mathrm{N}} = 11.3$ K. On the basis of non-equilibrium dynamical magnetic behaviour complemented with DFT calculations, it is illustrated that the magnetic ground state of the compound is magnetically frustrated where different possible spin configurations (AFM, FM, and FiM) with nearly degenerate ground-state energies compete with each other. Due to the simultaneous presence of strong spin-frustration and bond-disorder in the crystal structure, a spin-glass-like state develops below $T_{\mathrm{B}} \sim 4.8$ K, in this compound. The detailed studies on low-temperature non-equilibrium dynamical behavior, including magnetic relaxation, aging phenomena along with magnetic memory effect both in ZFC and FC conditions, confirm the short-range glassy state formation in this metallic compound. The dynamics of the non-equilibrium spin-frozen state are better described by the hierarchical description over the droplet model for spin-glasses.

Conflicts of interest

The authors declare that they have no known competing financial interests or personal relationships that could have appeared to influence the work reported in this paper.

Data availability

All the raw files of the data presented in this manuscript that support the findings of this present work are available from the corresponding author upon request. Contact: spakhira.phy@gmail.com.

Acknowledgements

A significant portion of this study has been conducted and supported through CMPID project at SINP and funded by the Department of Atomic Energy (DAE), Govt. of India. The authors express gratitude to Shibasis Chatterjee and Tridib Das for their technical support during the SEM & EDX measurements. We are thankful to Anish Karmahapatra for technical support during XRD measurements. Partial support for the research at Ames National Laboratory was provided by the U.S. Department of Energy, Office of Basic Energy Sciences, Division of Materials Sciences and Engineering. Iowa State University operates Ames National Laboratory for the U.S. Department of Energy under Contract No. DE-AC02-07CH11358. N.L. acknowledges the Council of Scientific and Industrial Research (CSIR), New Delhi for PPMS facility through XII Five Year Plan project MULTIFUN (CSC-0101) and thankful to the Director, CSIR-CECRI for the support (CECRI/PESVC/Pubs/2023-107).

References

1 S. Pakhira, C. Mazumdar, M. Avdeev, R. N. Bhowmik, and R. Ranganathan, *Journal of Alloys and Compounds*, 2019, **785**, 72-79.

2 T. Del Rose, A. K. Pathak, Y. Mudryk and V. K. Pecharsky, *Journal of Materials Chemistry C*, 2021, **9**, 181–188.

3 M. Khan, A. K. Pathak, Y. Mudryk, K. A. Gschneidner, Jr. and V. K. Pecharsky, *Journal of Materials Chemistry C*, 2017, **5**, 896-901.

4 S. Pakhira, C. Mazumdar, R. Ranganathan, and M. Avdeev, *Scientific Reports*, 2017, **7**, 7367.

5 S. Pakhira, C. Mazumdar, A. Basu, R. Ranganathan, R. N. Bhowmik, and B. Satpati, *Scientific Reports*, 2018, **8**, 14870.

6 R. Mallik, E. V. Sampathkumaran, and P. L. Paulose, *Solid State Communications*, 1998, **106**, 169-172.

7 D. X. Li, S. Nimori, Y. Shiokawa, Y. Haga, E. Yamamoto, and Y. Onuki, *Physical Review B*, 2003, **68**, 012413.

8 I. M. Siouris, I. P. Semitelou, J. K. Yakinthos, R. R. Arons, and W. Schäfer, *Journal of Magnetism and Magnetic Materials*, 2001, **226**, 1128-1130.

9 Y. Zhang, D. Guo, Y. Yang, S. Geng, X. Li, Z. Ren, and G. Wilde, *Journal of Alloys and Compounds*, 2017, **702**, 546-550.

10 N. Kase, T. Muranaka, and J. Akimitsu, *Journal of Magnetism and Magnetic Materials*, 2009, **321**, 3380-3383.

11 K. Ghosh, C. Mazumdar, R. Ranganathan, and S. Mukherjee, *Scientific Reports*, 2015, **5**, 15801.

12 R. Nirmala, A. V. Morozkin, A. K. Nigam, J. Lamsal, W. B. Yelon, O. Isnard, S. A. Granovsky, K. K. Bharathi, S. Quezado, and S. K. Malik, *Journal of Applied Physics*, 2011, **109**, 07A716.

13 S. Blundell, *Magnetism in condensed matter*, 2003, American Association of Physics Teachers.

14 V. K. Anand, D. T. Adroja, and A. D. Hillier, *Physical Review B*, 2012, **85**, 014418.

15 J. Kroder, K. Manna, D. Kriegner, A. S. Sukhanov, E. Liu, H. Borrmann, A. Hoser, J. Gooth, W. Schnelle, D. S. Inosov, G. H. Fecher, and C. Felser, *Physical Review B*, 2019, **99**, 174410.

16 J. E. Greedan, *Journal of Materials Chemistry*, 2001, **11**, 37-53.

17 D. Zhang, Z. Hou and W. Mi, *Journal of Materials Chemistry C*, 2022, **10**, 7748–7770.

18 B. Martínez, X. Obradors, F. Sandiumenge, and A. Labarta, *Springer*, 1997, **414**.

19 R. Moessner and A. P. Ramirez, *Physics Today*, 2006, **59**, 24-29.

20 L. Balents, *Nature*, 2010, **464**, 199-208.

21 J. Wen, S. L. Yu, S. Li, W. Yu, and J. X. Li, *npj Quantum Materials*, 2019, **4**, 12.

22 V. Lohani, C. Hickey, J. Masell, and A. Rosch, *Physical Review X*, 2019, **9**, 041063.

23 V. Ukleev, K. Karube, P. M. Derlet, C. N. Wang, H. Luetkens, D. Morikawa, A. Kikkawa, L. Mangin-Thro, A. R. Wildes, Y. Yamasaki, Y. Yokoyama, L. Yu, C. Piamonteze, N. Jaouen, Y. Tokunaga, H. M. Rnnow, T. Arima, Y. Tokura, Y. Taguchi, and J. S. White, *npj Quantum Materials*, 2021, **6**, 40.

24 Y. Hu, X. Chi, X. Li, Y. Liu, and A. Du, *Scientific Reports*, 2017, **7**, 16079.

25 Y. Zhou, *National Science Review*, 2019, **6**, 210-212.

26 B. Dupé, G. Bihlmayer, M. Böttcher, S. Blügel, and S. Heinze, *Nature Communications*, 2016, **7**, 11779.

27 X. Zhang, Y. Zhou, K. M. Song, T. E. Park, J. Xia, M. Ezawa, X. Liu, W. Zhao, G. Zhao, and S. Woo, *Journal of Physics: Condensed Matter*, 2020, **32**, 143001.

28 W. Kang, Y. Huang, X. Zhang, Y. Zhou, and W. Zhao, *Proceedings of the IEEE*, 2016, **104**, 2040-2061.

29 C. Tien, L. Luo, and J. S. Hwang, *Physical Review B*, 1997, **56**, 11710.

30 Z. J. Mo, J. Shen, X. Q. Gao, Y. Liu, C. C. Tang, J. F. Wu, F. X. Hu, J. R. Sun, B. G. Shen, *Journal of Alloys and Compounds*, 2015, **626**, 145-149.

31 D. X. Li, S. Nimori, Y. Shiokawa, Y. Haga, E. Yamamoto, Y. Onuki, *Solid State Communications*, 2001, **120**, 227-232.

32 S. Pakhira, A. K. Kundu, R. Ranganathan, and C. Mazumdar, *Journal of Physics: Condensed Matter*, 2018, **30**, 215601.

33 S. Pakhira, C. Mazumdar, and R. Ranganathan, *Journal of Magnetism and Magnetic Materials*, 2020, **512**, 167055.

34 M. Kundu, S. Pakhira, R. Choudhary, D. Paudyal, N. Lakshminarasimhan, M. Avdeev, S. Cottrell, D. Adroja, R. Ranganathan, and C. Mazumdar, *Scientific Reports*, 2021, **11**, 13245.

35 M. Kundu, S. Pakhira, R. Choudhary, S. Gupta, S. Chakraborty, N. Lakshminarasimhan, R. Ranganathan, D. D. Johnson, and C. Mazumdar, *Physical Review B*, 2023, **107**, 094421.

36 M. Kundu, S. Pakhira, D. Paudyal, N. Lakshminarasimhan, R. Ranganathan, and C. Mazumdar, *Intermetallics*, 2022, **151**, 107730.

37 S. Pakhira, C. Mazumdar and R. Ranganathan, *Journal of Physics: Condensed Matter*, 2017, **29**, 505801.

38 T. Kurumaji, T. Nakajima, M. Hirschberger, A. Kikkawa, Y. Yamasaki, H. Sagayama, H. Nakao, Y. Taguchi, T. Arima, and Y. Tokura, *Science*, 2019, **365**, 914-918.

39 R. Kumar, K. K. Iyer, P. L. Paulose, and E. V. Sampathkumaran, *Physical Review B*, 2020, **101**, 144440.

40 S. Chakraborty, S. Gupta, S. Pakhira, R. Choudhary, A. Biswas, Y. Mudryk, V. K. Pecharsky, D. D. Johnson, and C. Mazumdar, *Physical Review B*, 2022, **106**, 224427.

41 J. Rodríguez-Carvajal, *Physica B*, 1993, **192**, 55-69.

42 S. Pakhira, C. Mazumdar, R. Ranganathan, and S. Giri, *Physical Chemistry Chemical Physics*, 2018, **20**, 7082-7092.

43 S. Pakhira, C. Mazumdar, R. Ranganathan, S. Giri, and M. Avdeev, *Physical Review B*, 2016, **94**, 104414.

44 S. Pakhira, R. N. Bhowmik, M. Avdeev, R. Ranganathan, and C. Mazumdar, *Intermetallics*, 2020, **124**, 106874.

45 B. Kanrar, P. D. Babu, S. Kaity, G. Ravikumar, N. L. Mishra, *Journal of Alloys and Compounds*, 2021, **870**, 159325.

46 S. Pakhira, C. Mazumdar, R. Ranganathan, and S. Giri, *Journal of Alloys and Compounds*, 2018, **742**, 391-401.

47 V. K. Anand and D. C. Johnston, *Physical Review B*, 2015, **91**, 184403.

48 E. Gopal, *Springer Science+Business Media*, 2012,.

49 M. Kundu, C. Mazumdar, R. Ranganathan, and M. D. Raychaudhury, *Journal of Magnetism and Magnetic Materials*, 2019, **489**, 165452.

50 V. V. Romaka, G. Rogl, V. Buršíková, J. Buršík, H. Michor, A. Grytsiv, E. Bauer, G. Giester, and P. Rogl, *Dalton Transactions*, 2022, **51**, 361-374.

51 K. A. Denault, J. Brgoch, S. D. Klob, M. W. Gaultois, J. Siewenie, K. Page, and R. Seshadri, *ACS Applied Materials & Interfaces*, 2015, **7**, 7264-7272.

52 C. Mazumdar, K. Ghosh, S. Ramakrishnan, R. Nagarajan, L. C. Gupta, G. Chandra, B. D. Padalia, and R. Vijayaraghavan, *Physical Review B*, 1994, **50**, 13879.

53 Y. Sun, M. B. Salamon, K. Garnier, and R. S. Averback, *Physical Review Letters*, 2003, **91**, 167206.

54 M. Sasaki, P. E. Jonsson, H. Takayama, and H. Mamiya, *Physical Review B*, 2005, **71**, 104405.

55 D. S. Fisher and D. A. Huse, *Physical Review B*, 1988, **38**, 373.

56 D. S. Fisher and D. A. Huse, *Physical Review B*, 1988, **38**, 386.

57 W. L. McMillan, *Journal of Physics C: Solid State Physics*, 1984, **17**, 3179.

58 V. S. Dotsenko, *Journal of Physics C: Solid State Physics*, 1985, **18**, 6023.

59 E. Vincent, J. Hammann, M. Ocio, J. P. Bouchaud, L. F. Cugliandolo, *Springer*, 1997, **184**.

60 P. E. Blöchl, *Physical Review B*, 1994, **50**, 17953.

61 G. Kresse and D. Joubert, *Physical Review B*, 1999, **59**, 1758.

62 G. Kresse and J. Furthmüller, *Physical Review B*, 1996, **54**, 11169.

63 J. P. Perdew, K. Burke, and M. Ernzerhof, *Physical Review Letters*, 1996, **77**, 3865.

64 D. P. Kozlenko, E. Burzo, P. Vlaic, S. E. Kichanov, A. V. Rutkauskas and B. N. Savenko, *Scientific Reports*, 2015, **5**, 8620.

Data Availability Statement

All the raw files of the data presented in this manuscript that support the findings of this present work are available from the corresponding author upon request.

Contact: spakhira.phy@gmail.com